

# Optimum Electrical and Optical Properties of Transparent Conducting Oxide for Cu(In,Ga)Se<sub>2</sub> Photovoltaic Module Applications

Yosuke Abe,\* Takahito Nishimura, and Akira Yamada

Herein, the transparent conducting oxide (TCO) characteristics of the window layer as a factor in the decrease of conversion efficiency from lab-scale cells to modules are focused on. Then, an optical model and a circuit model are constructed based on measured data, and TCO parameters are investigated to optimize Cu(In,Ga)Se<sub>2</sub> (CIGS) module characteristics. Simulations assuming ZnO:Al and ZnO:B as the TCO, which are commonly used in CIGS modules with a substrate structure, show that the range of the TCO parameters to obtain high efficiency is limited. In particular, the optimum values of module characteristics are separated into high-carrier density/thin-film region with a smooth surface and low-carrier density/thick-film region with a textured surface for the TCO layer. In addition, simulations assuming a high-mobility TCO and a wide-gap CIGS absorber to boost conversion efficiency reveal that the wide-gap CIGS absorber mitigates the effects of resistance losses and free carrier absorption due to the TCO, thereby expanding the design range of the carrier density in the TCO layer.

resistance loss. Hence, a device design to reduce sheet resistance ( $R_{\text{sheet}}$ ) of the TCO layer is required.  $R_{\text{sheet}}$  can be expressed as follows

$$R_{\text{sheet}} = \frac{1}{en\mu d} \quad (1)$$

where  $e$ ,  $n$ ,  $\mu$ , and  $d$  are electron charge, carrier density, mobility, and film thickness, respectively. As shown in Equation (1),  $R_{\text{sheet}}$  can be lowered by increasing  $n$  or  $d$ . However, high  $n$  and/or  $d$  lead to deterioration of transparency in the TCO since free carrier absorption at longer wavelengths reduces transmittance, which results in a low-short-circuit current density ( $J_{\text{sc}}$ ) of the solar cells. Therefore, high  $\mu$  is needed to realize low  $R_{\text{sheet}}$ , while maintaining high transparency. The CIGS solar cells have the TCO layer formed on


## 1. Introduction

Cu(In,Ga)Se<sub>2</sub> (CIGS) is one of the most promising materials as a light-absorbing layer in thin-film solar cells, characterized by its high-optical absorption coefficient and tunability of the bandgap ( $E_g$ ) (1.00–1.68 eV).<sup>[1]</sup> The CIGS solar cells have achieved a power conversion efficiency (PCE) of 23.35%<sup>[2]</sup> in lab-scale cells. However, the PCE has been limited to 19.8 % in large-scale modules with the aperture areas of 665 cm<sup>2</sup><sup>[3]</sup> or 24.2 cm<sup>2</sup>,<sup>[4]</sup> where the decrease in performance due to integration has become a problem. In particular, the fill factor (FF) of CIGS modules is lower than that of CIGS lab-scale cells, and therefore, we focused on the characteristics of the transparent conducting oxide (TCO) for the window layer in this regard. In lab-scale solar cells, when the current is collected from the surface electrode, lateral current flow through the TCO is small, and the resistance loss in the TCO layer is relatively unproblematic. Nevertheless, in the case of the module shown in **Figure 1**, the current flows laterally across the TCO layer with a large scale, resulting in significant

the CIGS and n-type buffer layers, that is, substrate structure, and hence it has been reported that the properties of the CIGS/buffer layer junction deteriorate during the high-temperature deposition for the TCO layer.<sup>[5–7]</sup> Thus, the mainstream in the TCOs for the application of the CIGS solar cells is Al-doped ZnO (ZnO:Al) with  $\mu$  of 16–24 cm<sup>2</sup> V<sup>−1</sup> s<sup>−1</sup><sup>[8–11]</sup> deposited by magnetron sputtering at a temperature of 150 °C or below and B-doped ZnO (ZnO:B) with  $\mu$  of 24–37 cm<sup>2</sup> V<sup>−1</sup> s<sup>−1</sup><sup>[10,12]</sup> deposited by metal–organic chemical vapor deposition (MOCVD) at a substrate temperature of 160–170 °C. The ZnO:Al has a c-axis orientation<sup>[13]</sup> with a flat surface, while ZnO:B has an a-axis orientation<sup>[14]</sup> with a textured surface.<sup>[15]</sup>

As mentioned earlier, the degradation of PCE by integration for the solar cell modules has become an issue, but there is little knowledge of comprehensive CIGS module design that consistently takes into account the device structure from the physical properties of each layer. In this study, an optical model and a circuit model were combined and the effects of the electrical and the optical characteristics of the TCO on the module characteristics were investigated. Although there is a trade-off between the optical and the electrical properties of the TCO, the optimum parameters in the CIGS modules have never been disclosed quantitatively. In this regard, we conducted a comprehensive theoretical analysis focusing on the relationship between the optical and the electrical characteristics of the TCO to obtain design guidelines for the actual CIGS modules with the  $E_g$  of 1.1 eV. For the TCO layers, the ZnO:Al with the flat surface and the ZnO:B with the textured surface were assumed, and

Y. Abe, T. Nishimura, A. Yamada  
Department of Electrical and Electronic Engineering  
Tokyo Institute of Technology  
2-12-1 Ookayama, Meguro-ku, Tokyo 152-8550, Japan  
E-mail: abe.y.bc@m.titech.ac.jp

 The ORCID identification number(s) for the author(s) of this article can be found under <https://doi.org/10.1002/pssa.202300641>.

DOI: 10.1002/pssa.202300641

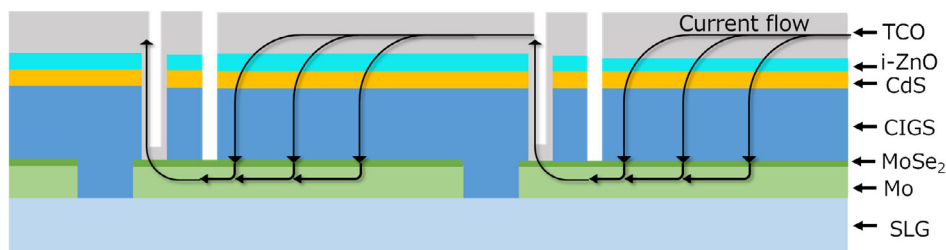


**Figure 1.** Structure of a typical CIGS module.

Tauc–Lorentz model<sup>[16]</sup> and Drude model<sup>[17]</sup> were combined to calculate a complex refractive index. The optical model to obtain a photocurrent based on the complex refractive index was designed by e-ARC software,<sup>[18]</sup> and then the obtained photocurrent was incorporated into the circuit model of a 160-series module using LTspice<sup>[19]</sup> to realize a module analysis that takes into account the optical and the electrical characteristics of the TCO layers. Here, diode parameters used in the circuit model were based on the measured values of the CIGS modules.

In addition, the simulations were also performed assuming a high- $\mu$  TCO considering the ongoing research on H-doped  $\text{In}_2\text{O}_3$  ( $\text{In}_2\text{O}_3:\text{H}$ ) with high  $\mu$  above  $100 \text{ cm}^2 \text{ V}^{-1} \text{ s}^{-1}$  deposited at temperatures below  $200^\circ\text{C}$ .<sup>[20,21]</sup> Particularly, the  $\mu$  of about  $50 \text{ cm}^2 \text{ V}^{-1} \text{ s}^{-1}$  for  $\text{In}_2\text{O}_3:\text{H}$  has been achieved without intentional heating.<sup>[20,21]</sup> When assuming the high- $\mu$  TCO, the  $E_g$  of the CIGS layer was widened from 1.1 to 1.4 eV. The relationship between the electrical and the optical properties of the TCO and a wide-gap absorber was analyzed, suggesting the design guidelines for actual modules.

## 2. Simulation Procedure

The module characteristics were simulated considering the increase in series resistance ( $R_s$ ) due to the integration and transparency of the TCO. **Figure 2** shows the simulation flow. The module structure has 120 cm width, 84.8 cm length, and 160 series cells (Figure 2a). The width of the active area, dead area, and TCO/Mo contact area per single cell were set to 5 mm, 0.3 mm, and  $50 \mu\text{m}$ , respectively (Figure 2b). The photocurrent per single cell was calculated by e-ARC (Figure 2c), which estimates the external quantum efficiency (EQE) spectrum for the solar cells with the TCO/i-ZnO/CdS/CIGS/MoSe<sub>2</sub>/Mo structure. The complex refractive indexes were taken from ref. [22] for Mo, i-ZnO, and  $\text{MgF}_2$ , ref. [23] for MoSe<sub>2</sub>, ref. [22,24] for CdS, and ref. [25] for CIGS, respectively. The  $E_g$  of CIGS was set to 1.1 eV or 1.4 eV, and it is assumed to be uniform in the direction of the film thickness.  $[\text{Ga}]/([\text{Ga}]+[\text{In}])$  (GGI) was set to 0.2 and 0.6 for the  $E_g$  of 1.1 and 1.4 eV, respectively, where the reported complex refractive indexes in the CIGS with the GGI ratios of

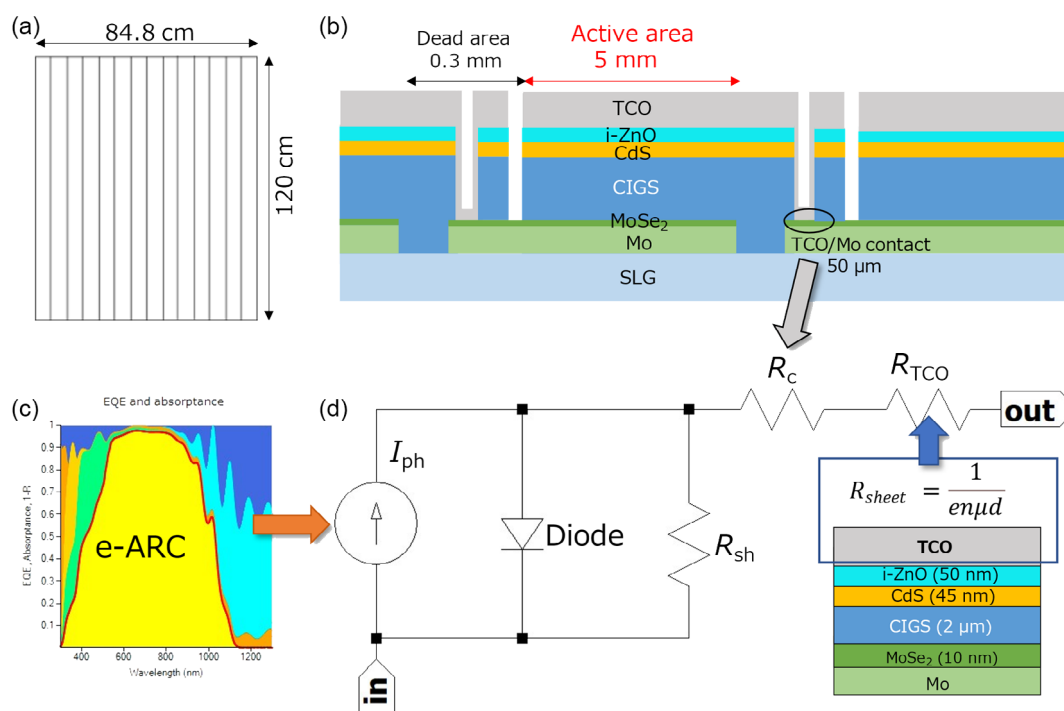


**Figure 2.** Simulation flow: a) planar and b) cross-sectional view of the structure for the CIGS module used in the simulation, c) EQE calculated from e-ARC, and d) single-cell equivalent circuit.

0.2 and 0.6<sup>[25]</sup> were used in this simulation. Then, the photocurrent was evaluated by e-ARC. The simulation for the module with the wide-gap CIGS absorber with the  $E_g$  of 1.4 eV is discussed in Section 3.3.

LTspice software was utilized to calculate the characteristics of the CIGS modules. The equivalent circuit for the single cell was designed, as shown in Figure 2d, and then the circuit models of 160 cells were connected in series to reproduce the CIGS modules, where  $I_{ph}$ ,  $R_{sh}$ ,  $R_c$ , and  $R_{TCO}$  denote photocurrent, shunt resistance, contact resistance at the TCO/Mo interface, and series resistance of the TCO layers, respectively. Here,  $R_{sh}$ ,  $R_c$ , and  $R_{TCO}$  were fixed at 500  $\Omega$ , 6.67 m $\Omega$ , and  $R_{sheet} \times 0.5/120$ , respectively, according to the measured values for the actual CIGS modules.  $I_{ph}$  per single cell calculated by e-ARC (Figure 2c) and  $R_{TCO}$  calculated from Equation (1) were input into the single-cell equivalent circuit in Figure 2d, and eventually, the performance of the CIGS modules was characterized.

The ZnO:Al with the flat surface and  $\mu$  of 20 cm<sup>2</sup> V<sup>-1</sup> s<sup>-1</sup> or the ZnO:B with the textured surface and  $\mu$  of 30 cm<sup>2</sup> V<sup>-1</sup> s<sup>-1</sup> was assumed as the TCO layers.  $n$  and  $d$  were varied in the range of 1–15  $\times 10^{20}$  cm<sup>-3</sup> and 0.05–1.5  $\mu$ m, respectively. **Figure 3** shows the device structures used in e-ARC with (a) ZnO:Al and (b) ZnO:B layers applied as the TCO layers. It was assumed that MgF<sub>2</sub> was formed on the surface of the ZnO:Al as an antireflection coating layer. Meanwhile, a surface roughness layer was introduced on ZnO:B, assuming the formation of the textured surface, whose thickness corresponds to 5% of the total thickness for the ZnO:B layer.

The optical constants were calculated using the Tauc–Lorentz model, which accounts for inter-band transitions, and the Drude model, which accounts for free carrier absorption. The Tauc–Lorentz model parameters,<sup>[16]</sup>  $A$  and  $C$ , were fixed to 40 and 0.8, respectively, and  $E_g$  widening due to the Burstein–Moss effect<sup>[26]</sup> was considered. In addition,  $E_0$  which represents a peak position of absorption was set to  $E_g + 0.2$ . For the Drude model, dielectric function ( $\epsilon(\omega)$ ) can be expressed by Equation (2).

$$\epsilon(\omega) = \epsilon_{\infty} - \frac{\omega_p^2}{\omega^2 + i\omega\omega_{\tau}} \quad (2a)$$

$$\omega_p^2 = \frac{ne^2}{\epsilon_0 m^*} \quad (2b)$$

$$\omega_{\tau} = \frac{e}{\mu m^*} \quad (2c)$$

In Equation (2),  $\omega_p$ ,  $\omega_{\tau}$ ,  $\epsilon_0$ ,  $\epsilon_{\infty}$ ,  $m^*$  are plasma frequency, damping frequency, permittivity of free space, high-frequency dielectric constant, and effective mass of electron. Here,  $\epsilon_{\infty}$  decreases and  $m^*$  increases with increasing  $n$ .<sup>[26]</sup>

Bruggman's effective medium approximation<sup>[28]</sup> shown in Equation (3) was utilized to calculate  $\epsilon(\omega)$  of the roughness layer on the ZnO:B with the textured surface.

$$f_a \frac{\epsilon_a - \epsilon}{\epsilon_a + 2\epsilon} + f_b \frac{\epsilon_b - \epsilon}{\epsilon_b + 2\epsilon} = 0 \quad (3a)$$

$$f_a + f_b = 1 \quad (3b)$$

In Equation (3),  $f_a$ ,  $f_b$ ,  $\epsilon_a$ , and  $\epsilon_b$  are mixing ratio and dielectric function for substances, a and b, respectively.  $\epsilon$  is dielectric function of the mixed substance. In this study, substances, a and b, were defined as air and ZnO:B, and the mixing ratio of  $f_a$  and  $f_b$  was 50%.

In Section 3.3, the high- $\mu$  TCO is discussed utilizing the same structure shown in Figure 3a assuming In<sub>2</sub>O<sub>3</sub>:H with the flat surface instead of ZnO:Al. The reported value of  $\mu$  about 50 cm<sup>2</sup> V<sup>-1</sup> s<sup>-1</sup> for In<sub>2</sub>O<sub>3</sub>:H deposited at room temperature<sup>[20]</sup> was used.

The diode parameters used for the CIGS modules were obtained to be applied in the single-cell equivalent circuit shown in Figure 2d. The current–voltage ( $I$ – $V$ ) characteristics were measured for a sample of the CIGS modules with  $E_g$  of 1.1 eV, which was provided by Solar Frontier K.K., and an ideality factor ( $A$ ) and a reverse-saturation current density ( $J_0$ ) were estimated by analyzing the  $I$ – $V$  curves.<sup>[29]</sup> It was found that the loss of the open-circuit voltage ( $V_{OC}$ ) per single cell was about 0.4 V in the CIGS modules with  $E_g$  of 1.1 eV, where the loss of  $V_{OC}$  is defined by  $E_g/q - V_{OC}$ . In this simulation, it was assumed that the bulk defects and CdS/CIGS interface properties remained unchanged despite of the widening of  $E_g$  from 1.1 to 1.4 eV in the CIGS. Therefore,  $A$  and  $J_0$  were adjusted so that the loss of  $V_{OC}$  is equal to 0.4 V, which is the same as  $E_g$  of 1.1 eV. The diode parameters used in this simulation are shown in **Table 1**.

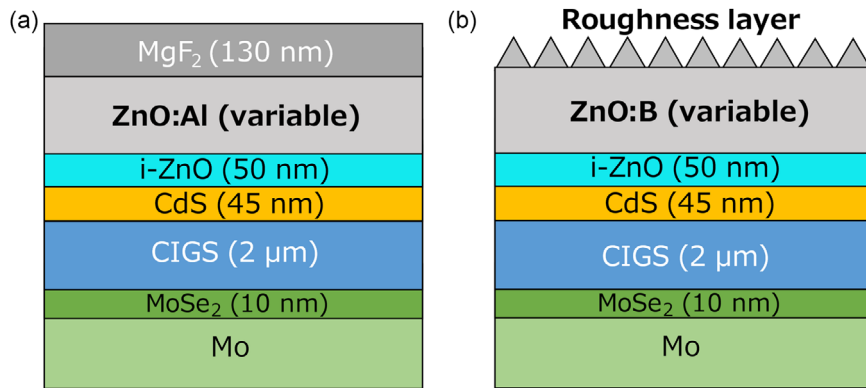


**Figure 3.** Solar cell structures used in e-ARC with TCO layers of a) flat surface ZnO:Al with  $\mu$  of 20 cm<sup>2</sup> V<sup>-1</sup> s<sup>-1</sup>, and b) textured surface ZnO:B with  $\mu$  of 30 cm<sup>2</sup> V<sup>-1</sup> s<sup>-1</sup>. The film thickness of each layer is shown in parentheses.

**Table 1.** Diode parameters applied in the single-cell equivalent circuit.

CIGS band gap ( $E_g$ ) [eV]	Ideality factor ( $A$ )	Reverse-saturation current density ( $J_0$ ) [ $\text{A cm}^{-2}$ ]
1.1	1.55	$1.14 \times 10^{-9}$
1.4	1.45	$7.24 \times 10^{-14}$

### 3. Results and Discussion

#### 3.1. Flat Surface ZnO:Al with $\mu$ of $20 \text{ cm}^2 \text{ V}^{-1} \text{ s}^{-1}$

To discuss the influence of the properties in ZnO:Al, the performance of the CIGS modules was simulated with varying  $d$  and  $n$  of ZnO:Al as the TCO layer. **Figure 4** depicts the mappings of the simulated  $J_{\text{SC}}$ , FF, and PCE as a function of  $d$  and  $n$  for the flat surface ZnO:Al layers with  $\mu$  of  $20 \text{ cm}^2 \text{ V}^{-1} \text{ s}^{-1}$  in the CIGS modules. The different colors of the background in each mapping diagram correspond to the values of  $R_{\text{sheet}}$  for the ZnO:Al layer, which decrease with varying the colors from white to black, as shown in the color bar.

In **Figure 4a**, the FF was improved with decreasing  $R_{\text{sheet}}$  according to the increase in the  $d$  and/or  $n$  in the ZnO:Al layer. The FF depends on the only  $R_{\text{sheet}}$  of the ZnO:Al layer since the

diode parameters of  $A$  and  $J_0$  were fixed, namely, no effects of the defects or the other factors in the devices. Therefore, the FF saturated at around 0.76 in the region of thicker  $d$  and higher  $n$ . Meanwhile, in **Figure 4b**, the highest  $J_{\text{SC}} \approx 35 \text{ mA cm}^{-2}$  was observed at the small values of  $d$  and  $n$  (e.g.,  $d \approx 0.3 \mu\text{m}$  and  $n \approx 3 \times 10^{20} \text{ cm}^{-3}$ ), whereas  $J_{\text{SC}}$  was monotonically decreased with increasing  $d$  and/or  $n$ , which resulted in the lower  $J_{\text{SC}} \approx 13 \text{ mA cm}^{-2}$  at the thicker  $d \approx 1.5 \mu\text{m}$  and higher  $n \approx 1.5 \times 10^{21} \text{ cm}^{-3}$ . This is due to the effect of free carrier absorption by the ZnO:Al with the increase in  $d$  and  $n$ . Remarkably,  $J_{\text{SC}}$  drastically decreased at the region of  $d < 0.3 \mu\text{m}$  and  $n < 3 \times 10^{20} \text{ cm}^{-3}$ , which is caused by the higher  $R_{\text{sheet}}$  ( $> 100 \Omega \text{ sq}^{-1}$ ) in the ZnO:Al layer.

It was disclosed that relatively high PCE over 13% was obtained at the region of high  $n$  of  $5\text{--}13 \times 10^{20} \text{ cm}^{-3}$  and thin  $d$  of  $0.2\text{--}0.5 \mu\text{m}$  or at the region of low  $n$  of  $3\text{--}5 \times 10^{20} \text{ cm}^{-3}$  and thick  $d$  of  $0.5\text{--}0.9 \mu\text{m}$  as shown in **Figure 4c** due to the trade-off between the electrical and the optical properties of ZnO:Al. Finally, the highest PCE of 13.3% was obtained at  $n$  of  $7\text{--}9 \times 10^{20} \text{ cm}^{-3}$  and  $d$  of  $0.3\text{--}0.4 \mu\text{m}$ . It was consequently revealed that a large fluctuation of PCE exists along with  $d$  direction, suggesting that uniformity of the ZnO:Al thickness is required for the mass production of the large-scale CIGS modules.

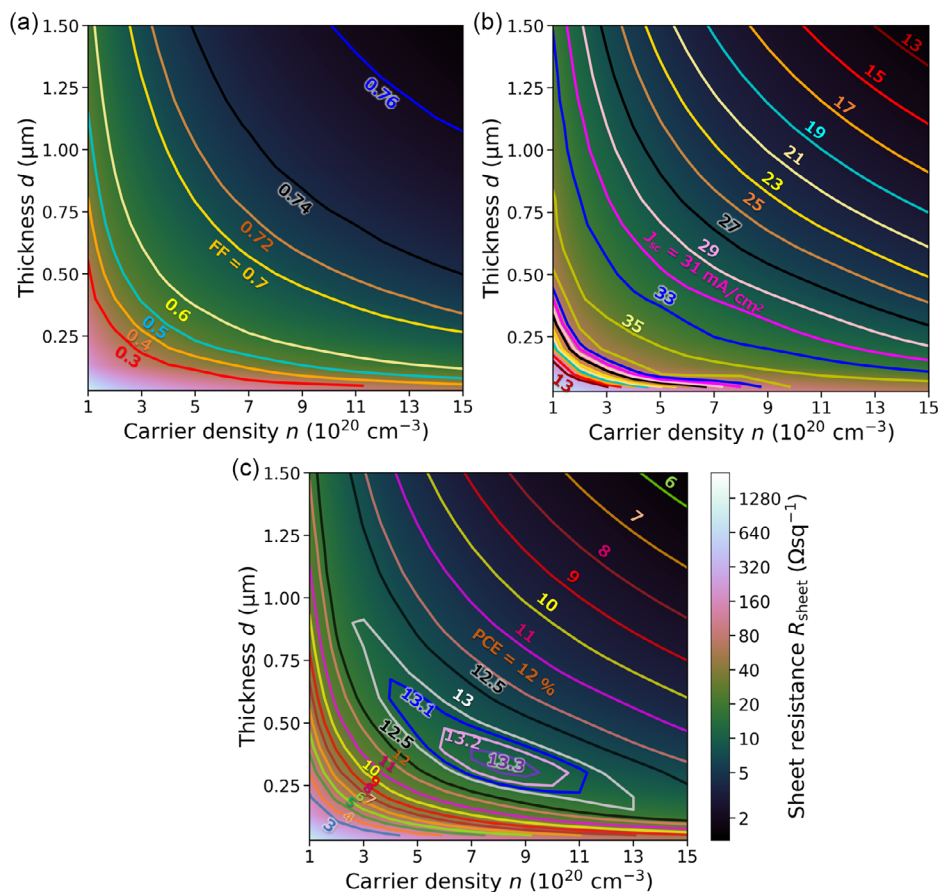


**Figure 4.** Mappings of simulated module characteristics of a) FF, b)  $J_{\text{SC}}$ , and c) PCE as a function of  $d$  and  $n$  for the flat surface ZnO:Al with  $\mu$  of  $20 \text{ cm}^2 \text{ V}^{-1} \text{ s}^{-1}$  as TCO layers.



### 3.2. Textured Surface ZnO:B with $\mu$ of $30 \text{ cm}^2 \text{ V}^{-1} \text{ s}^{-1}$

The simulation was performed for the CIGS modules with varying  $d$  and  $n$  of the textured surface ZnO:B with  $\mu$  of  $30 \text{ cm}^2 \text{ V}^{-1} \text{ s}^{-1}$  as the TCO layers. The FF was increased and  $J_{\text{SC}}$  was decreased with increasing  $d$  and/or  $n$ , as shown in Figure S1, Supporting Information, where its trend corresponds to the ZnO:Al TCO layers, as discussed in Figure 4a,b.

Figure 5 shows (a) the mapping of PCE with varying  $d$  and  $n$  and (b) PCE as a function of  $d$  for the ZnO:B TCO layers. As shown in Figure 5a, high PCE over 14% was obtained at the regions with saturated FF  $\approx 0.7$  and relatively high  $J_{\text{SC}} \approx 33 \text{ mA cm}^{-2}$ . Intriguingly, it was disclosed that the highest value of PCE ( $>14.5\%$ ) was separated into the region of high  $n$  of  $11\text{--}15 \times 10^{20} \text{ cm}^{-3}$  and thin  $d$  of  $0.10\text{--}0.25 \mu\text{m}$  and the region of low  $n$  of  $1\text{--}2 \times 10^{20} \text{ cm}^{-3}$  and thick  $d$  of  $1.0\text{--}1.5 \mu\text{m}$ . The region with the relatively low  $R_{\text{sheet}}$  value of  $\approx 8 \Omega \text{ sq}^{-1}$  with the high PCE existed along with the hyperbolic shapes according to Equation (1), suggesting that the effect of the resistance loss is almost the same in the region. Therefore, the separation of the regions with the highest PCE  $>14.5\%$  was caused by the  $J_{\text{SC}}$  values. The surface roughness layer of the ZnO:B was incorporated into the simulation assuming that the textures were formed on the surface during the film growth, where the texture acts as an antireflection layer in the condition of the thick  $d$ . Therefore, at the region of low  $n$  of  $1\text{--}2 \times 10^{20} \text{ cm}^{-3}$  and thick  $d$  of  $1.0\text{--}1.5 \mu\text{m}$ , the high  $J_{\text{SC}}$  can be obtained due to the antireflection effect by the surface roughness layer on ZnO:B. Meanwhile, if  $d$  is thin enough, the effect of free carrier absorption can be mitigated even in high  $n$ . Eventually, there are two options in the surface roughness layer on the TCO to achieve the low  $R_{\text{sheet}}$  and high  $J_{\text{SC}}$ . First, the  $d$  should be thicker in the low  $n$  value to realize the antireflection effect. Second, the  $d$  should be thinner in the high  $n$  value to reduce free carrier absorption.

Figure 5b shows PCE as a function of  $d$  at the low  $n$  of  $2 \times 10^{20} \text{ cm}^{-3}$  and high  $n$  of  $1.4 \times 10^{21} \text{ cm}^{-3}$ . In the high  $n$ , the high PCE over 14% was observed at the narrow range of  $d$  of  $0.10\text{--}0.30 \mu\text{m}$ . On the other hand, in the low  $n$ , the high PCE over 14% was obtained at the wide range of  $d$  above

$0.85 \mu\text{m}$ , indicating that a wide margin of the thickness for the ZnO:B can be obtained. From an industrial standpoint, it is desirable to form the films in thin  $d$  region with high  $n$  to achieve high throughput and low cost. However, in the deposition methods with nonuniformity of film thickness, such as MOCVD, the thick  $d$  of  $1.0\text{--}1.5 \mu\text{m}$  with the low  $n$  of  $1\text{--}2 \times 10^{20} \text{ cm}^{-3}$  is required to stabilize the performances in the in-plane direction for the large-scale CIGS modules.

### 3.3. Simulations Assuming Wide-Gap CIGS Absorber and High- $\mu$ $\text{In}_2\text{O}_3\text{:H}$ TCO Layers

#### 3.3.1. Advantages of Wide-Gap CIGS Absorber for Solar Cell Modules

Figure 6 shows the optical properties of the TCO calculated by the Drude model and the  $E_g$  of CIGS, where  $T$ ,  $R$ , and  $A$  denote transmittance, reflectance, and absorption, respectively. Since the TCO is a degenerated semiconductor due to the high  $n$ , plasma reflection by the free carriers occurs at the region of the longer wavelength, and resonance absorption occurs due

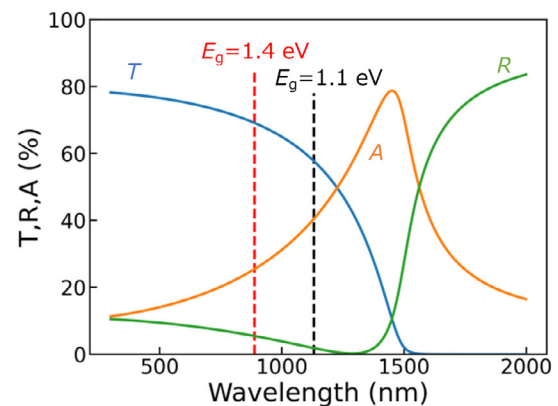


**Figure 6.** Optical properties of the TCO calculated by the Drude model utilizing  $n$  of  $8 \times 10^{20} \text{ cm}^{-3}$ ,  $\mu$  of  $50 \text{ cm}^2 \text{ V}^{-1} \text{ s}^{-1}$ , and  $d$  of  $1.0 \mu\text{m}$ .  $T$ ,  $R$ , and  $A$  denote transmittance, reflectance, and absorption, respectively.

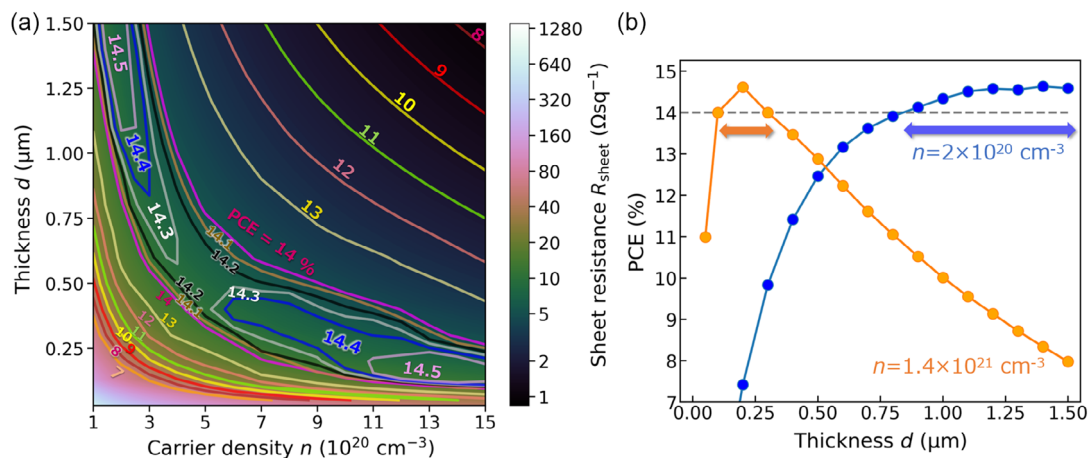


**Figure 5.** a) Mapping of simulated PCE as a function of  $d$  and  $n$ , and b) PCE as a function of  $d$  at low  $n$  of  $2 \times 10^{20} \text{ cm}^{-3}$  and high  $n$  of  $1.4 \times 10^{21} \text{ cm}^{-3}$  for the textured surface ZnO:B with  $\mu$  of  $30 \text{ cm}^2 \text{ V}^{-1} \text{ s}^{-1}$  as TCO layer.

to the collective motion of the free carriers. The issue here is that the resonance absorption (free carrier absorption) occurs over a broad range due to the decrease in  $\mu$  and the increase in  $d$ , extending to the wavelength range utilized in solar cells, as shown in Figure S2, Supporting Information.

The dashed line in Figure 6 shows the wavelength of 1128 and 886 nm equivalent to  $E_g$  of 1.1 and 1.4 eV for the CIGS absorbers. The  $A$  of 40% at the wavelength of 1128 nm is higher than that of 25% at the wavelength of 886 nm, leading to the lower  $T$  of 58% at 1128 nm than that of 68% at 886 nm. The result suggests that the CIGS absorber with the narrow  $E_g$  of 1.1 eV is strongly affected by free carrier absorption in the TCO layers, which is related to the decrease in  $J_{SC}$ . In contrast, the CIGS absorber with the wide  $E_g$  of 1.4 eV would suppress the influence of the free carrier absorption.

### 3.3.2. Simulation Results

The simulations were conducted utilizing the device structure shown in Figure 3a with the  $\text{In}_2\text{O}_3\text{:H}$  with the flat surface and  $\mu$  of  $50 \text{ cm}^2 \text{ V}^{-1} \text{ s}^{-1}$ , where the  $E_g$  of CIGS absorbers was set to 1.1 eV or 1.4 eV. The highest PCE is theoretically expected in the single-junction solar cells with  $E_g$  of 1.4 eV due to the matching of the sunlight spectrum.<sup>[30]</sup> However, the PCE in experiments decreases with increasing Ga contents for the CIGS solar cells due to the deep defect levels in the CIGS absorbers and the CIGS/buffer interface properties, which result in the low PCE at high  $E_g$  of 1.4 eV.<sup>[31,32]</sup> In this work, as explained in Section 2, the influences of the defects of the CIGS and the CdS/CIGS interface properties were not considered to discuss only the blueshift of the absorption edge associated with the widening of the  $E_g$ . Figure 7 and Table 2 show the simulated  $I$ - $V$  curves and solar cell characteristics, respectively, for the modules with the  $E_g$  of 1.1 and 1.4 eV in the CIGS absorbers. As shown in the result, the PCE increases with the widening of the  $E_g$  to 1.4 eV.

Figure 8 depicts the simulated mapping diagram of the PCE as a function of  $d$  and  $n$  for the  $\text{In}_2\text{O}_3\text{:H}$  with  $\mu$  of  $50 \text{ cm}^2 \text{ V}^{-1} \text{ s}^{-1}$  as TCO layers for the CIGS modules with the  $E_g$  of (a) 1.1 and (b) 1.4 eV. The mapping diagrams of FF and  $J_{SC}$  are summarized in Figure S3 (Supporting Information). The  $V_{OC}$  for each single cell

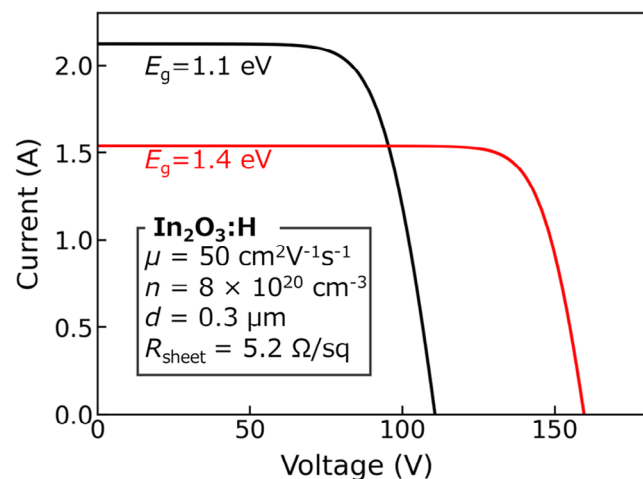


**Figure 7.**  $I$ - $V$  curve simulation results.

**Table 2.** Simulated solar cell parameters for the modules in the  $E_g$  of 1.1 and 1.4 eV for the CIGS absorbers.

$E_g$ [eV]	$J_{SC}$ [ $\text{mA cm}^{-2}$ ]	$V_{OC}$ [V]	FF	PCE [%]
1.1	35.4	111 (0.69/cell)	0.711	16.4
1.4	25.7	160 (1.0/cell)	0.802	19.4

was higher by about 0.3 V in the  $E_g$  of 1.4 eV than  $E_g$  of 1.1 eV, as shown in Table 2, and hence FF in the  $E_g$  of 1.4 eV is potentially higher than the  $E_g$  of 1.1 eV. The FF improves with decreasing  $R_{sheet}$  for both  $E_g$  of 1.1 and 1.4 eV in Figure S3a,b (Supporting Information). For the  $E_g$  of 1.4 eV, the FF was notably improved with increasing  $d$  and  $n$ , and its increment was relatively large compared with the  $E_g$  of 1.1 eV. This is due to the effect of the  $E_g$  widening, which leads to the lowered current, consequently mitigating the resistance losses. In Figure S3c,d (Supporting Information), it was found the reduction of the  $J_{SC}$  with increasing  $d$  and  $n$  was small in the  $E_g$  of 1.4 eV compared with the  $E_g$  of 1.1 eV. The results indicate that the blueshift at the absorption edge by  $E_g$  widening reduces the influence of the free carrier absorption at longer wavelengths. To improve FF, the  $R_{sheet}$  should be reduced by increasing  $d$  and  $n$ , whereas  $J_{SC}$  is unintentionally reduced due to the free carrier absorption at a longer-wavelength region. The wider  $E_g$  of 1.4 eV alleviated this trade-off by suppression of the influence of the free carrier absorption.

In Figure 8a,b, the high PCE over 19.3% in the wide  $E_g$  of 1.4 eV was observed at the region of high  $n$  of  $5\text{--}13 \times 10^{20} \text{ cm}^{-3}$  and thin  $d$  of  $0.1\text{--}0.4 \text{ }\mu\text{m}$ , although the high PCE over 16.3% in the narrow  $E_g$  of 1.1 eV was obtained at the region of relatively low  $n$  of  $2\text{--}9 \times 10^{20} \text{ cm}^{-3}$  and thicker  $d$  of  $0.25\text{--}0.95 \text{ }\mu\text{m}$ . Remarkably, for the  $E_g$  of 1.4 eV, the region with the high PCE was expanded along with the direction of  $n$ . Figure 8c shows PCE as a function of  $n$  with the fixed  $d$  of  $0.3 \text{ }\mu\text{m}$ . The dashed lines correspond to the values of 98% relative to the highest PCE of 16.1 and 19.1% in  $E_g$  of 1.1 and 1.4 eV, respectively. It was disclosed that the values over 98% relative to the highest PCE were achieved in the wide  $n$  region of  $4\text{--}15 \times 10^{20} \text{ cm}^{-3}$  for the  $E_g$  of 1.4 eV and in the narrow  $n$  region of  $5\text{--}11 \times 10^{20} \text{ cm}^{-3}$  for the  $E_g$  of 1.1 eV, respectively. For the narrow  $E_g$  of 1.1 eV, the effect of  $J_{SC}$  reduction due to free carrier absorption clearly appeared at the high  $n$  ( $>10 \times 10^{20} \text{ cm}^{-3}$ ) despite the reduced  $R_{sheet}$ , resulting in a decrease in PCE. Meanwhile, by introducing the wide  $E_g$  of 1.4 eV, the optical loss by free carrier absorption was suppressed in spite of the high  $n$  ( $>10 \times 10^{20} \text{ cm}^{-3}$ ) while remaining low  $R_{sheet}$ , finally achieving high PCE under the high design flexibility for the TCO carrier density.

## 4. Conclusion

The module characteristics of the CIGS solar cells were calculated using e-ARC for the optical calculations and LTspice for the circuit calculations. The CIGS solar cells have a substrate structure, which limits TCO film formation conditions such as substrate temperature, and the simulations were conducted considering the current TCO characteristics.

There was a trade-off between FF and  $J_{SC}$  due to the two requirements of the  $R_{sheet}$  and the transparency for the TCO,

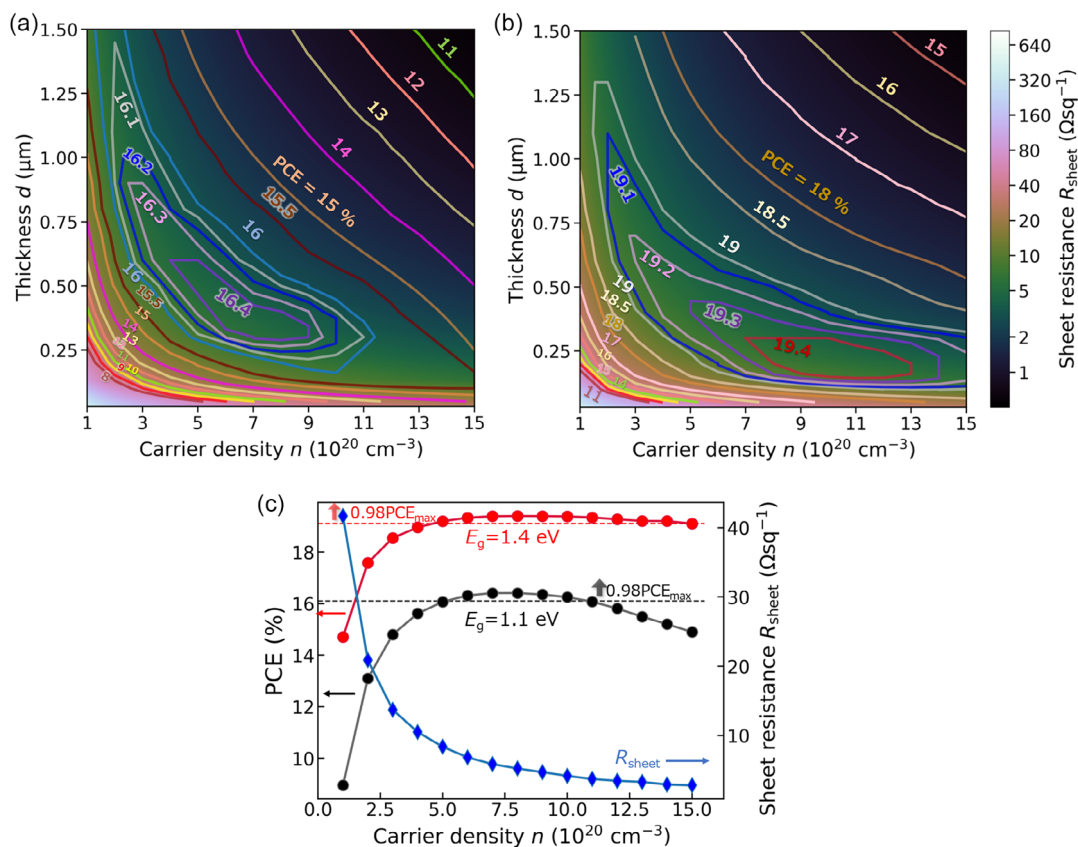


**Figure 8.** Mappings of the simulated PCE in a)  $E_g$  of 1.1 eV and b)  $E_g$  of 1.4 eV for the CIGS absorbers as a function of  $d$  and  $n$  for the flat surface  $\text{In}_2\text{O}_3\text{:H}$  with  $\mu$  of  $50 \text{ cm}^2 \text{ V}^{-1} \text{ s}^{-1}$  as the TCO layers, and c) PCE as a function of  $n$  with the fixed thickness  $d$  of 0.3  $\mu\text{m}$ .

consequently limiting the conditions with the high PCE. Assuming the  $\mu$  of  $20 \text{ cm}^2 \text{ V}^{-1} \text{ s}^{-1}$  with the flat surface  $\text{ZnO:Al}$  as the TCO layer, the highest PCE was obtained at the relatively high  $n$  of  $7\text{--}9 \times 10^{20} \text{ cm}^{-3}$  and thin  $d$  of 0.3–0.4  $\mu\text{m}$ , and the PCE fluctuated significantly in the direction of  $d$  variation. Assuming the textured  $\text{ZnO:B}$  with  $\mu$  of  $30 \text{ cm}^2 \text{ V}^{-1} \text{ s}^{-1}$  as the TCO layer, the highest PCE was found to be separated into the region of high  $n$  of  $11\text{--}15 \times 10^{20} \text{ cm}^{-3}$  and thin  $d$  of 0.1–0.25  $\mu\text{m}$  and the region of low  $n$  of  $1\text{--}2 \times 10^{20} \text{ cm}^{-3}$  and thick  $d$  of 1.0–1.5  $\mu\text{m}$ . Although the high  $n$  of  $11\text{--}15 \times 10^{20} \text{ cm}^{-3}$  and thin  $d$  of 0.1–0.25  $\mu\text{m}$  region is industrially desirable for high throughput and low cost, since PCE fluctuates significantly with changes of  $d$ , it is thought that the low  $n$  of  $1\text{--}2 \times 10^{20} \text{ cm}^{-3}$  and thick  $d$  of 1.0–1.5  $\mu\text{m}$  region is needed to stabilize PCE. In any case, uniformity of  $d$  is an important issue in large-scale CIGS modules.

Finally, the relationship between the electrical and the optical properties of the TCO and the wide-gap absorber was analyzed. It was revealed that the widening of  $E_g$  from 1.1 to 1.4 eV suppressed the optical loss by the free carrier absorption under high  $n$  ( $>10 \times 10^{20} \text{ cm}^{-3}$ ) and achieved high design flexibility with respect to TCO carrier density.

## Supporting Information

Supporting Information is available from the Wiley Online Library or from the author.

## Acknowledgements

This work was supported by the New Energy and Industrial Technology Development Organization (NEDO), and the authors would like to thank all parties involved. The authors extend sincere appreciation to Solar Frontier K.K. for generously providing the samples used in this study.

## Conflict of Interest

The authors declare no conflict of interest.

## Data Availability Statement

The data that support the findings of this study are available from the corresponding author upon reasonable request.

## Keywords

CIGS, free carrier absorptions, sheet resistances, solar cells, solar cell modules, transparent conductive oxides

Received: August 25, 2023

Revised: October 5, 2023

Published online: November 22, 2023

- [1] T. Maeda, R. Nakanishi, M. Yanagita, T. Wada, *Jpn. J. Appl. Phys.* **2020**, 59, SGGF12.
- [2] M. Nakamura, K. Yamaguchi, Y. Kimoto, Y. Yasaki, T. Kato, H. Sugimoto, *IEEE J. Photovolt.* **2019**, 9, 1863.
- [3] AVANCIS, AVANCIS Enhances Its Own World Record for the Efficiency of CIGS Thin Film Solar Modules, *Press Release*, **2022**. <https://www.avancis.de/en/magazine/pr-efficiency>. (accessed: 5 October 2023).
- [4] T. Kato, A. Handa, T. Yagioka, T. Matsuura, K. Yamamoto, S. Higashi, J. L. Wu, K. F. Tai, H. Hiroi, T. Yoshiyama, T. Sakai, H. Sugimoto, *IEEE J. Photovolt.* **2017**, 7, 1773.
- [5] S. Ichi Shimakawa, Y. Hashimoto, S. Hayashi, T. Satoh, T. Negami, *Sol. Energy Mater. Sol. Cells* **2008**, 92, 1086.
- [6] A. Koprek, O. Cojocaru-Miredin, R. Wuerz, C. Freysoldt, B. Gault, D. Raabe, *IEEE J. Photovolt.* **2017**, 7, 313.
- [7] S. Kijima, T. Nakada, *Appl. Phys. Express* **2008**, 1, 0750021.
- [8] T. Koida, J. Nishinaga, Y. Ueno, H. Higuchi, H. Takahashi, M. Iioka, Y. Kamikawa, H. Shibata, S. Niki, *Prog. Photovolt.* **2019**, 27, 491.
- [9] T. Koida, Y. Ueno, J. Nishinaga, Y. Kamikawa, H. Higuchi, M. Iioka, H. Takahashi, H. Shibata, S. Niki, *Thin Solid Films* **2019**, 673, 26.
- [10] T. Koida, J. Nishinaga, H. Higuchi, A. Kurokawa, M. Iioka, Y. Kamikawa-Shimizu, A. Yamada, H. Shibata, S. Niki, *Thin Solid Films* **2016**, 614, 79.
- [11] A. C. Badgujar, B. S. Yadav, G. K. Jha, S. R. Dhage, *ACS Omega* **2022**, 7, 14203.
- [12] K. Maejima, T. Koida, H. Sai, T. Matsui, K. Saito, M. Kondo, T. Takagawa, *Thin Solid Films* **2014**, 559, 83.
- [13] M. Berginski, J. Hüpkens, M. Schulte, G. Schöpe, H. Stiebig, B. Rech, M. Wuttig, *J. Appl. Phys.* **2007**, 101, 074903.
- [14] W. W. Wenas, A. Yamada, K. Takahashi, M. Yoshino, M. Konagai, *J. Appl. Phys.* **1991**, 70, 7119.
- [15] K. Y. Kou, Y. E. Huang, C. H. Chen, S. W. Feng, *Beilstein J. Nanotechnol.* **2016**, 7, 75.
- [16] G. E. Jellison, F. A. Modine, *Appl. Phys. Lett.* **1996**, 69, 371.
- [17] J. Steinhauser, S. Faÿ, N. Oliveira, E. Vallat-Sauvain, C. Ballif, *Appl. Phys. Lett.* **2007**, 90, 142107.
- [18] A. Nakane, H. Tampo, M. Tamakoshi, S. Fujimoto, K. M. Kim, S. Kim, H. Shibata, S. Niki, H. Fujiwara, *J. Appl. Phys.* **2016**, 120, 064505.
- [19] <http://www.linear.com/solutions/ltspace>. (accessed: 5 October 2023).
- [20] T. Koida, H. Fujiwara, M. Kondo, *Jpn. J. Appl. Phys, Part 2: Lett.* **2007**, 46, L685.
- [21] T. Koida, H. Fujiwara, M. Kondo, *Sol. Energy Mater. Sol. Cells* **2009**, 93, 851.
- [22] T. Hara, T. Maekawa, S. Minoura, Y. Sago, S. Niki, H. Fujiwara, *Phys. Rev. Appl.* **2014**, 2, 034012.
- [23] M. Richter, C. Schubbert, P. Eraerds, I. Riedel, J. Keller, J. Parisi, T. Dalibor, A. Avellan-Hampe, *Thin Solid Films* **2013**, 535, 331.
- [24] C. Jie, L. Jian, D. Sainju, K. D. Wells, N. J. Podraza, R. W. Collins, in *2006 IEEE 4th World Conf. on Photovoltaic Energy Conversion*, Waikoloa, HI **2006**, Vol. 1, p. 475.
- [25] S. Minoura, T. Maekawa, K. Kodaera, A. Nakane, S. Niki, H. Fujiwara, *J. Appl. Phys.* **2015**, 117, 195703.
- [26] H. Fujiwara, M. Kondo, *Phys. Rev. B: Condens. Matter Mater. Phys.* **2005**, 71, 075109.
- [27] Z. C. Jin, I. Hamberg, C. G. Granqvist, *J. Appl. Phys.* **1988**, 64, 5117.
- [28] D. E. Aspnes, *Thin Solid Films* **1982**, 89, 249.
- [29] S. S. Hegedus, W. N. Shafarman, *Prog. Photovolt. Res. Appl.* **2004**, 12, 155.
- [30] W. Shockley, H. J. Queisser, *J. Appl. Phys.* **1961**, 32, 510.
- [31] P. K. Paul, K. Aryal, S. Marsillac, S. A. Ringel, A. R. Arehart, in *2016 IEEE 43rd Photovoltaic Specialists Conf.*, Portland, OR **2016**, p. 2246.
- [32] H. A. Al-Thani, F. S. Hasoon, in *2021 IEEE 48th Photovoltaic Specialists Conf.*, Fort Lauderdale, FL **2021**, p. 2047.